Interference microscopy and Fourier fringe analysis applied to measuring the spatial refractive-index distribution

S. Kostianovski, S. G. Lipson, and E. N. Ribak

We have applied the technique of Fourier fringe analysis to microscopic interferograms of needle crystals that grow from a solution. We use a differential technique in which an empty field interferogram is compared with one that contains distortion and obscuration by the growing crystal, and we demonstrate both analytically and experimentally a phase shift sensitivity of 0.01 fringe with a spatial resolution of half of a fringe spacing (~ 1 μm). Following the analysis of the interferogram in two dimensions, we show that the three-dimensional refractive-index field around the crystal can be deduced, assuming that it is axially symmetric, by an iterative method.

Introduction

We describe a technique that we have developed to measure a three-dimensional field of refractive index by means of an interference microscope by using Fourier fringe analysis.[1–6] The practical application of the technique was to determine the concentration field around a needle crystal that grows from a supersaturated solution; this information is important in gaining a basic understanding of the phenomenon of dendritic growth.[7] However, we believe that the technique and its analysis have applications outside the field of crystal growth, and we present them here in a manner that will not require the reader's familiarity with our application. In particular, we present a careful analysis of the accuracy of the method and discuss the sources of error in the measurement and their correction in some detail.

The experiment is to be envisaged as follows. We have a refractive-index field $n(x, y, z)$ that exists within an externally bounded region and that may contain some internal obscurations (the growing crystal). In our case the external boundaries are two parallel planes at $z = \pm z_0$; the lower boundary is a plane mirror and the upper boundary is a thin optical window. The observation was made by using a Linnik interference microscope in reflected light. The interference measures the optical thickness at each point (x, y):

$$l(x, y) = \int_{-z_0}^{z_0} n(x, y, z) - 1 \mathrm{d}z. \tag{1}$$

This is done by observing the distortions of a fringe pattern that, under initial conditions in which $l(x, y) =$ constant, shows a set of nominally straight equally spaced fringes. We assume that in the region that interests us the spatial variations in n are small enough that the integration can be taken to be along a straight line as implied by Eq. (1).

Analysis of the fringe pattern is made so as to achieve the following aims. The first is to determine, as accurately as possible, the boundaries of the obscured area. The second is to measure the field $l(x, y)$. The third is to deduce from $l(x, y)$ a three-dimensional field $n(x, y, z)$ that is consistent with it and with a minimum of additional constraints (which of course will depend on the physical system being investigated and the boundary conditions). This is a problem in tomography.

Experimental System

The Linnik microscope, based on the Michelson interferometer, is shown in Fig. 1. It forms an image of the experimental cell that interferes with a plane wave, the two being imaged by identical 40× objectives. The interference fringes are localized in the plane of the mirrors. Although this type of interferometer is commonly used with white light, in this application we require quasi-monochromatic illumina-

The authors are with the Department of Physics, Technion–Israel Institute of Technology, Haifa 32000, Israel.

Received 5 August 1992.
0003-6935/93/254744-07$06.00/0.

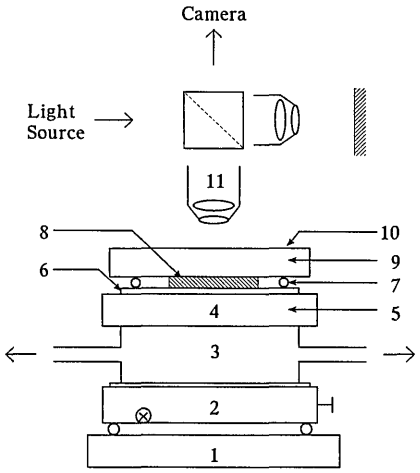

Fig. 1. Schematic diagram of the experimental system: 1, microscope stage; 2, tilting table; 3, water-cooled chamber; 4, thermoelectric (Peltier) coolers; 5, copper base; 6, thin mirror (sapphire); 7, wire spacers; 8, sample; 9, cover glass; 10, dry nitrogen flow (to prevent mist condensation); 11, Linnik interferometer.

tion so as to get a large number of fringes. We used a mercury discharge lamp with a filter at $\lambda = 5640$ Å; with such light, exact chromatic matching of the two objectives was unnecessary.

A typical cell thickness was $2z_0 = 28$ μm as determined by two soft copper wire spacers. The base mirror was of sapphire coated with Cr, and the window was a 0.1-mm glass cover slip 25 mm × 30 mm. The experiments[8] were done by placing a small drop of NH_4Cl solution in the center of the cell, cooling and inducing nucleation of needlelike crystals that grew at a typical velocity of 140 $\mu \cdot s^{-1}$.

Our aim was to measure the concentration field around the growing tip by using the refractive index as an indicator, with enough spatial resolution and to a sufficient degree of accuracy to differentiate between competing models for dendritic growth. The refractive index is related to solute concentration c and temperature T. The former relationship is linear:

$$n(c) = 1.3325 + 0.0019c, \quad (2)$$

and the dependence on T is ignored because it is very small around the temperature of the experiments (4 °C) and the boundary conditions were in any case isothermal.

Fringe Pattern Analysis

The observed optical path differences were somewhat less than one wavelength. This occurs because the experimental cell is necessarily thin to ensure that the fringes and crystal were both within the depth of focus. (By using a lower magnification and a thicker cell, Raz *et al.*[8] obtained path differences as large as three wavelengths but sacrificed spatial resolution.) We considered two possible methods for extracting phase information. The first was to use spatially incoherent illumination and to measure the intensity variations that result from the path-length changes when the interferometer is adjusted for uniform phase (one fringe across the whole field). The accuracy of this method is limited by intensity calibration, and one can clearly obtain diffraction-limited resolution. An alternative that we chose is Fourier fringe analysis,[1–6] which needs spatially coherent illumination and has less spatial resolution but allows a greater degree of precision in determining the phase (solute concentration).

We begin by arranging a uniform field $l(x, y) =$ constant that gives a dense set of straight fringes, with spacing $\Lambda = 2\pi/\omega_0$, by tilting the reference mirror of the interferometer. As was done by Takeda and Mutoh,[2] we record this interference pattern, denoted by $g_0(x, y)$, before the crystal growth begins (the empty field), since it includes all the instrumental effects such as nonplanar mirrors. After the initiation of crystal growth we observed a new interferogram $g(x, y)$ in which the fringes are distorted and part of the field is obscured by the growth crystal.

The principle of the Fourier technique is in fact exactly equivalent to holographic interferometry carried out digitally by using a Fourier hologram. We summarize it briefly in the form we use it, and Fig. 2 shows the stages diagrammatically. Denoting the normal to the fringes as the x axis,

$$g_0(x, y) = a(x, y) + 2b(x, y)\cos[\omega_0 x + \phi_0(x, y)], \quad (3)$$

where a, b, and ϕ_0 are functions that represent imperfections in the optics. The distorted field contains additional obscuration $d(x, y)$ and phase shift $\phi(x, y)$, both of which are of direct interest to us, and is

$$g(x, y) = d(x, y)\{a(x, y) + 2b(x, y)\cos[\omega_0 x + \phi(x, y) + \phi_0(x, y)]. \quad (4)$$

We write the Fourier transforms $G_0(u, v)$ and $G(u, v)$ of these two fields as, for example,

$$G_0(u, v) = A(u, v) + B(u, v) * [\delta(u - \omega_0)\delta(v) * P_0(u, v) + \delta(u + \omega_0)\delta(v) * P_0^*(-u, -v)], \quad (5)$$

where $P_0(u, v)$ is the transform of $\exp[i\phi_0(x, y)]$; otherwise capital letters symbolize transforms of lowercase symbols. Each of G_0 and G is centrosymmetric (because the functions g_0 and g are real) and has a zero-order peak and two first-order peaks around $u = \pm\omega_0$. The orders are not δ functions because of the functions a, b, etc. There are also higher orders at $u = \pm 2\omega_0, \pm 3\omega_0, \ldots$, but these result from nonlinearities in the recording and are small enough to be neglected. The next step is to shift one of the first orders to the origin of the Fourier plane and to remove all other orders. A detailed understanding of this is needed for quantitative analysis of the

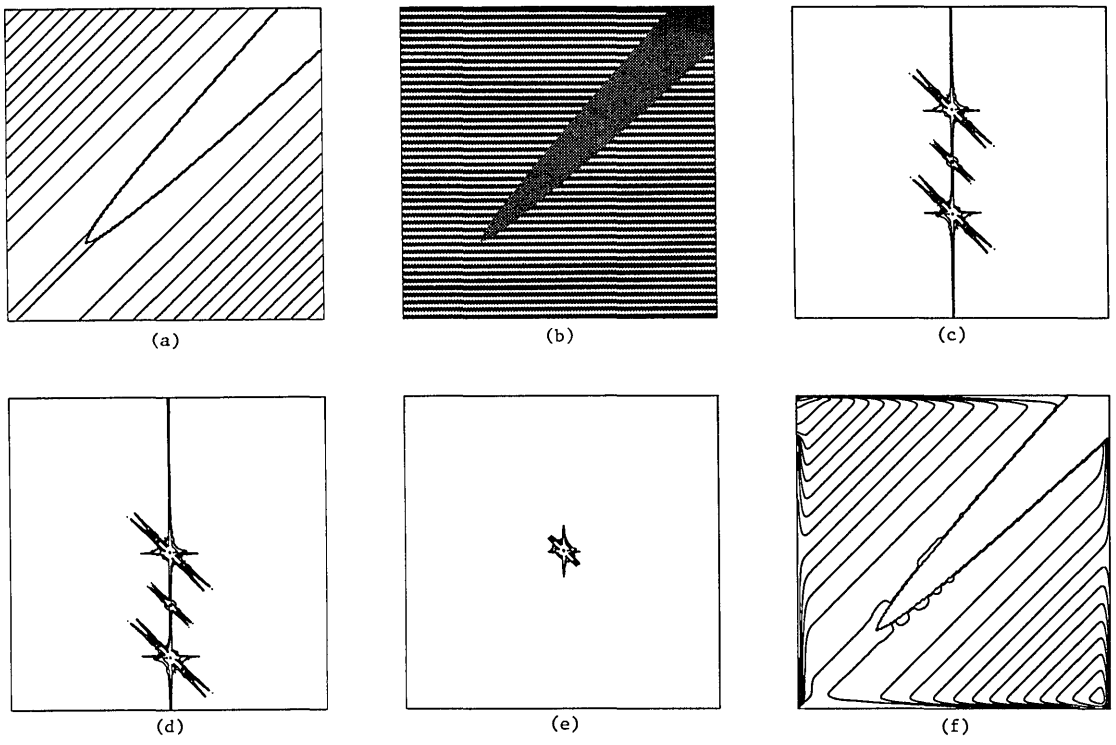

Fig. 2. Illustration of the Fourier plane operations: (a) contour map of the imposed phase variation and obstruction (contours at intervals of 0.02π), (b) the fringe field corresponding to (a), (c) Fourier transform of (b) (amplitude contours) with the origin at the center of the field, (d) transform shifted so that the first order is at the origin, (e) transform after removal of zero and minus first orders, (f) reconstructed contour map of phases with the same scale as (a).

method and is discussed below. Now we have, in principle, the new functions

$$G_0'(u, v) = 2B(u, v) * P_0(u, v), \tag{6}$$

$$G'(u, v) = 2B(u, v) * D(u, v) * P_0(u, v) * P(u, v). \tag{7}$$

The inverse transform of Eq. (6) is $g_0'(x, y)$ and that of Eq. (7) is $g'(x, y)$. We define their ratio as

$$r(x, y) = \frac{g'(x, y)}{g_0'(x, y)} = d(x, y)\exp[i\phi(x, y)]. \tag{8}$$

We are interested in two aspects of $r(x, y)$. We have

$$d(x, y) = |r(x, y)|, \tag{9}$$

$$\phi(x, y) = \text{phase}[r(x, y)]. \tag{10}$$

By thresholding d as obtained from Eq. (9) we can deduce the outline of the obscured area, and in the unobscured part Eq. (10) gives us the phase of the field.

Source and Magnitude of Phase Errors

Most previous analyses of the Fourier fringe technique have centered around the problem of locating 2π phase jumps.[2–4] This problem does not concern us since $\phi < 2\pi$ in our experiments. The phase $\phi(x, y)$ as determined by the procedure is not exact because of the need to define a window that separates the first order from the rest of the transform. The window tells us to accept all the transform within it and reject all that outside. However since the orders are continuous functions that extend throughout the Fourier plane, the window necessarily contains some of the outlying parts of the zero and even minus-first orders and also rejects some of the tail of the first order. By changing the size or shape of the window or using an apodization function (semitransparent window) we can alleviate the problem but not remove it completely. It is therefore important to estimate the size of the error introduced by the window and to look for methods to minimize it.

A second source of error arises from the presence of the obscured region. Unless the function $d(x, y)$ is centrosymmetrical, its transform D will not be real and it seems that the phase of D might get attached to ϕ. In fact this error can be dealt with quite easily once the boundary of the obscured region has been determined. This boundary is then used to blank out an identical obscured region from both g_0 and g. The same phase error then appears in both g_0' and g' and disappears when their ratio is taken in Eq. (8).

A third source of error comes from the fact that the processes involved are digital. If there is not a whole number of fringes in the field of view, the spatial frequency ω_0 is not at an integer point in the Fourier plane. However, the shift to the origin has to be rounded to a whole number. It is easy to see that

this can introduce a phase error that is linearly related to position in the field and can amount to as much as π at the edges. If both g_0 and g have exactly the same number of fringes, the error disappears when one calculates the ratio r, but in any case, once it is recognized one can easily subtract this error because it is linear.

To estimate the size of the errors and to determine how to minimize them we resort to a simple analytical model of a field in which we expect them to appear. This model uses a window apodized by a Gaussian function, which was chosen because its Fourier transform is real and nonzero, so that it cannot introduce spurious phase errors. In the analytical model the phase change is assumed to be uniform; this is obviously of little practical use but allows us to understand the origins of phase errors. More significant from the practical point of view is the confirmation of the analytical result by a simulation.

The field has fringes with spacing Λ in the x direction and a rectangular obscuration of dimensions $2a_0 \times 2b_0$. The phase of g is ϕ while that of g_0 is zero. We then have

$$g_0(x,y) = 1 + \cos \omega_0 x, \tag{11}$$

$$g(x,y) = [1 - \mathrm{rect}(x/a_0)\mathrm{rect}(y/b_0)][1 + \cos(\omega_0 x + \phi)]. \tag{12}$$

The transform of the latter is

$$G(u,v) = [\delta(u)\delta(v) - 4a_0b_0\,\mathrm{sinc}(a_0u)\mathrm{sinc}(b_0v)] * [\delta(u)\delta(v) + \tfrac{1}{2}\exp(-i\phi)\delta(u - \omega_0)\delta(v) + \tfrac{1}{2}\exp(i\phi)\delta(u + \omega_0)\delta(v)]. \tag{13}$$

This is illustrated by Fig. 3(a) in one dimension.

We create an apodized window around the first order by multiplying the transform in Eq. (13) by the Gaussian function $\exp\{-[(u - \omega_0)^2 + v^2]/2\sigma^2\}$. Then we translate the origin by $-\omega_0$ [Fig.3(b)]. We then have two contributions to the transform $G'(u, v)$: the original first order now centered at

$$G_1'(u,v) = \exp(-i\phi)[\tfrac{1}{2}\delta(u)\delta(v) - 2a_0b_0\,\mathrm{sinc}(a_0u) \times \mathrm{sinc}(b_0v)]\exp[-(u^2 + v^2)/2\sigma^2], \tag{14}$$

and the rejected zero order

$$G_2'(u,v) = -4a_0b_0\,\mathrm{sinc}[a_0(u - \omega_0)] \times \mathrm{sinc}(b_0v)\exp[-(u^2 + v^2)/2\sigma^2] + \exp[-(\omega_0^2/2\sigma^2)]\delta(u - \omega_0)\delta(v). \tag{15}$$

A third contribution from the minus first order is

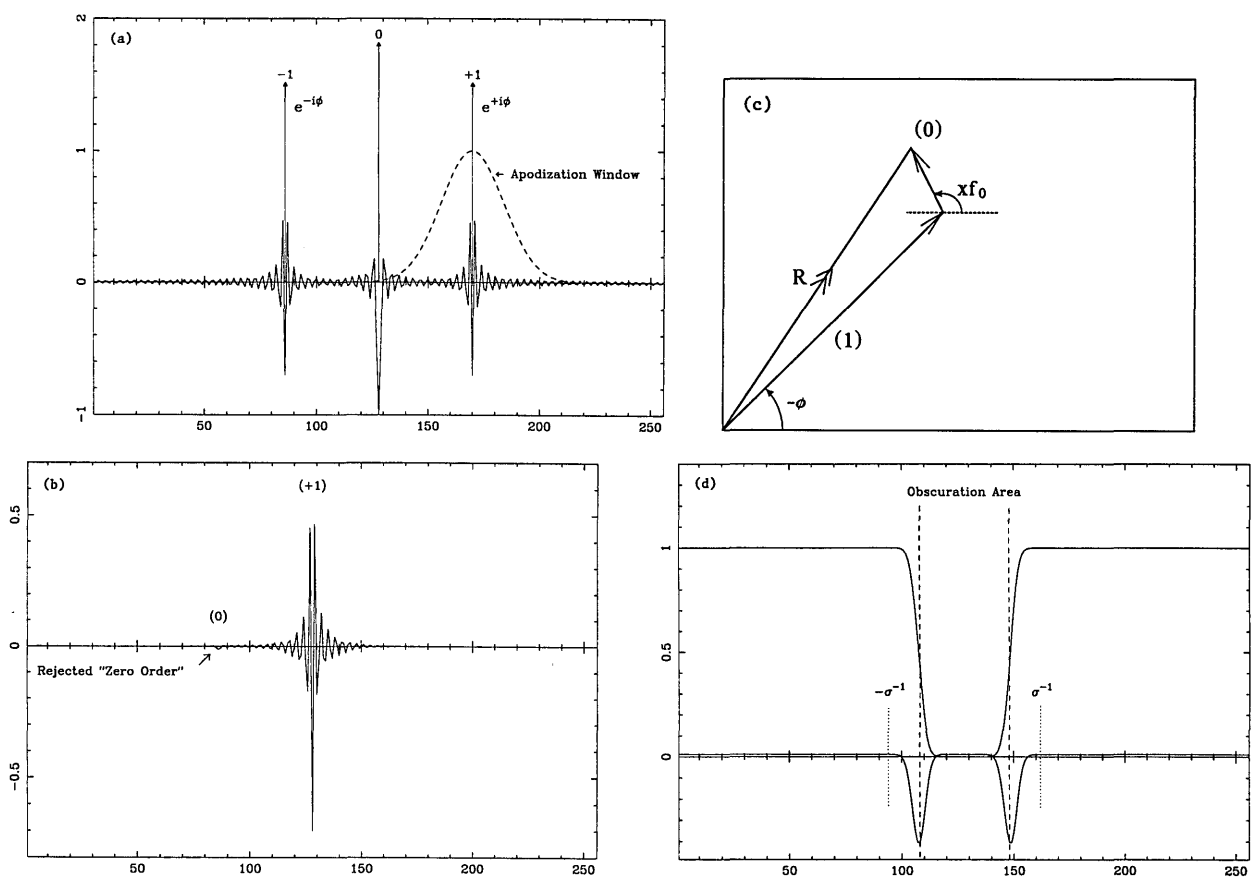

Fig. 3. Fourier transform of the model field: (a) in its initial form, (b) after the apodized window operation, (c) the two vectors that contribute to the phase field reconstruction, (d) comparison of the amplitudes of the two contributions to the reconstruction for $\sigma = \omega_0/3$.

neglected. Retransforming each term we have

$$g_1'(x,y) = \tfrac{1}{2}\exp(-i\phi)[1 - \mathrm{rect}(x/a_0)\mathrm{rect}(y/b_0)] * \frac{\sigma}{\sqrt{2\pi}}\exp[-(x^2+y^2)\sigma^2/2], \quad (16)$$

$$g_2'(x,y) = \exp(ix\omega_0)\exp(-\omega_0^2/2\sigma^2) - [\exp(ix\omega_0)\mathrm{rect}(x/a_0)\mathrm{rect}(y/b_0)] * \frac{\sigma}{\sqrt{2\pi}}\exp[-(x^2+y^2)\sigma^2/2]. \quad (17)$$

If we look at these two contributions as vectors in the complex plane, Fig 3(c), we see two vectors at angles $-\phi$ and $x\omega_0$, respectively. What we interpret as the phase is the angle of their resultant **R**. The error in angle that is introduced by the second term can be no greater than the ratio between their lengths (when they are at right angles) and can be zero if they are parallel ($x\omega_0 - \phi = n\pi$). The amplitudes of the two functions are illustrated as functions of x (at $y = 0$) in Fig. 3(d) for the case $\omega_0/\sigma = 3$. The following points should be clear from the diagram:

(a) In the field at a large distance ($\gg \sigma^{-1}$) from the edge of the obscuration, the maximum phase error is $\delta\phi = \exp(-\omega_0^2/2\sigma^2)$.

(b) Within a region $\sigma^{-1}/2$ of the edge it has a value that may be somewhat larger than the above, since the second term in Eq. (17) becomes comparable to the first. The numerical calculation illustrated by Fig. 3(d) suggests that the error may be an order of magnitude larger in this region.

(c) Within the obscuration the value is meaningless.

Now if we are interested in reducing the error, clearly ω_0/σ must be made as large as possible. However, since the transform G' is essentially restricted to a region of the Fourier plane of diameter σ, the spatial resolution of g' is σ^{-1}. Thus we pay for the accuracy of phase by degrading spatial resolution. A compromise situation is to choose $\omega_0/\sigma = 3$, which gives a far-field error in phase of $\exp(-9/2) = 0.01$ rad. The resolution of the reconstructed image is then 0.5 fringe, which is acceptable if the fringes are closely spaced. It is of course impossible to use a fringe spacing smaller than approximately 4 pixels because of sampling requirements.

Figure 2 illustrates an actual numerical example of the process. Figure 2(b) shows a field containing horizontal fringes obscured by a parabolic crystal with its axis at an angle to the fringes. The distorted field contains a phase ϕ varying with position in a Gaussian manner, with a maximum $\ll \pi/2$ rad; the value at each point is shown as a contour map in Fig. 2(a), in which the interval between the contours is 0.06 rad. The phase difference between the empty field and the distorted field is recovered by the Fourier technique and is shown in Fig. 2(f). One can see that errors are introduced around the edges of the frame and at the boundary of the crystal. The maximum error in the latter region, one pixel from the boundary, is found to be 0.08 rad., which is 0.05 fringe. However, if we exclude the region within one resolution distance (0.5 fringe) of the edge of the crystal, the maximum error is approximately 0.005 fringe.

Tomography

Now assume that we have obtained the best possible estimate of $\phi(x,y) = 2\pi l(x,y)/\lambda$, which represents the integrated value of $n(x,y,z)$ as in Eq. (1). In order to extract values of n in a slice of the three-dimensional system, we have to perform a tomographic inversion that generally involves much more input data than we have available (several directions of observation, for example). However, by assuming that the needle crystal and the surrounding field have axial symmetry within the confines of the flat cell, we can make the problem tractable. This assumption of isotropy is fairly realistic for the crystals that we are analyzing at present. It was not our intention in this research to develop tomographic algorithms, so we used an iterative technique that is easy to code although it may be less efficient than a direct method.[9] We have confirmed that the resultant $n(x,y,z)$ reproduces the input data when it is integrated by Eq. (1).

The assumption of axial symmetry as shown in Fig. 4 means that points such as B and D at the same radius from the axis are assumed to have the same value of n. It is then possible to look for a unique solution to the problem. For a section normal to the axis (which now defines the y axis), the integral

$$l(x,y) = 2\int_A^E n(x,y,z)\mathrm{d}z = 2\int_A^F n(x',y,0)\left(\frac{\mathrm{d}z}{\mathrm{d}x'}\right)\mathrm{d}x', \quad (18)$$

where D is at $(x',y,0)$, x' and z is related by $x'^2 = x^2 + z^2$. Then

$$l(x,y) = 2\int_A^F n(x',y,0)x'(x'^2 - x^2)^{-1/2}\mathrm{d}x'. \quad (19)$$

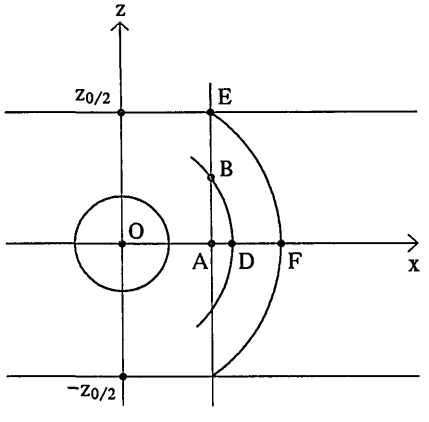

Fig. 4. Geometry of the tomographic analysis.

We solve this equation by iteration by using a field proportional to l as an initial guess for n in the plane $z = 0$, i.e., $n(x', y, 0) = \alpha_0 l(x, y)$, where $\alpha_0 = 1/2z_0$. For each x outside the obscuration we calculate a new value $l_1(x, y)$:

$$l_1(x, y) = 2\alpha_0 \int_A^F l(x', y)x'(x'^2 - x^2)^{-1/2}dx'. \quad (20)$$

We now calculate a new position-dependent value

$$\alpha_1(x, y) = \alpha_0 l(x, y)/l_1(x, y). \quad (21)$$

Now the main contribution to the integral in Eq. (20) comes from the region in which $x' \simeq x$ and so the product $\alpha_1(x, y)l(x, y)$ should be a better approximation to $n(x, y)$ than was the original $\alpha_0 l(x, y)$. So a new value $l_2(x, y)$ is calculated:

$$l_2(x, y) = 2\int_A^F \alpha_1(x', y)l(x', y)x'(x'^2 - x^2)^{-1/2}dx'. \quad (22)$$

Once again, a new $\alpha_2(x, y) = \alpha_0 l(x, y)/l_2(x, y)$ is calculated and the integration repeated. This is iterated until the indicator

$$\chi_n^2 = \iint \frac{[l_n(x, y) - l(x, y)]^2}{l^2(x, y)}\,dxdy \quad (23)$$

ceases to fall.

It is clear that the value of $\alpha(x, y)l(x, y)$, which is obtained this way, is a field $n(x, y)$ that is consistent with the data and axial symmetry; it is possible, although unlikely, that there is another solution. In practice, the value converges after three or four iterations. Only positions (x, y) for which the extreme point E has an equivalent F in the axial plane can be treated this way. Thus the output field is somewhat restricted with respect to the original data field; this will be clear from the example that follows.

Figure 5 shows an example of the data treated by this procedure. The complete interferogram contained 64k pixels and is shown in Fig. 5(a). The optical path contour map $l(x, y)$ is shown in Fig. 5(b), as calculated with a Gaussian window with $\sigma = \omega_0/3$. The final result, which is the central slice of the refractive index, translated to a solute concentration by using Eq. (2), is shown in Fig. 5(c). The axial symmetry, a necessary assumption for carrying out the algorithm, has been impressed on the data as can be seen. It is clear that the refractive index n at any other point in the cell can be found, but this adds no useful information.

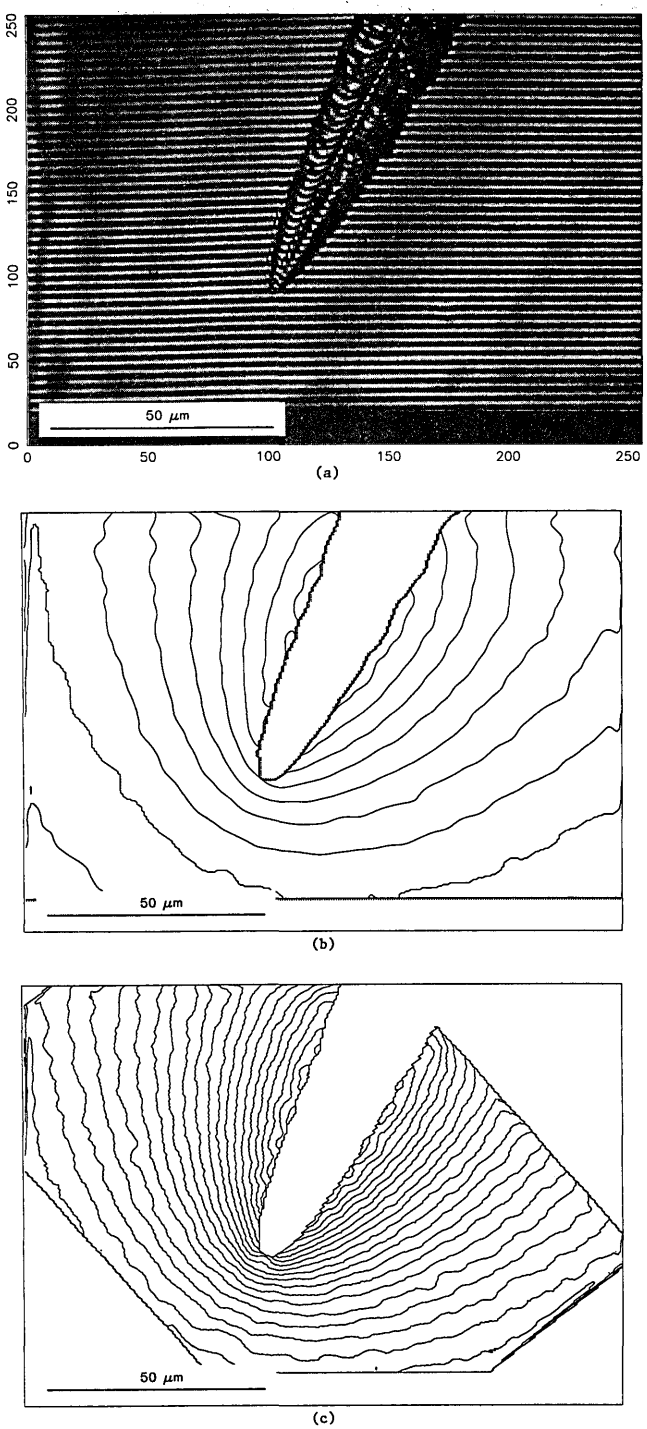

Fig. 5. Results obtained for a needle crystal growing from supersaturated solution: (a) the interferogram, (b) the optical path $l(x, y)$ (contour map at intervals of 0.1π), (c) the concentration field $c(x, y, 0)$ in the plane that contains the axis of the crystal [contour map at intervals of 0.1% from Eq. (2)]. Note the impressed axial symmetry and the restricted region of the field for which calculations were possible.

Conclusions

We have shown that the technique of Fourier fringe analysis, when used in a differential mode to find the distortion of an interference pattern, can give a phase accuracy of approximately 0.01 fringe. The price of such accuracy is a degradation of the spatial resolution to approximately half of a fringe spacing. By using the data from such an analysis, applied to interference micrographs of crystals growing from solution, we have been able to deduce the three-

dimensional solute field around the crystal, on the assumption that it has axial symmetry, with a spatial resolution of approximately 1 μm. In future work we shall try to develop techniques that will allow relaxation of the assumption of axial symmetry in the tomographic treatment of the data.

We acknowledge many useful and enlightening discussions with E. Ben-Jacob and O. Shochet, with whom the crystal-growth applications of this research are being developed. The research was carried out with the support of the Fund for Basic Research, administered by the Israel Academy for the Arts and Sciences and the U.S.–Israel Binational Science Foundation.

References

1. M. Takeda, H. Ina, and S. Kobayashi, "Fourier-transform method of fringe-pattern analysis for computer-based tomography and interferometry," J. Opt. Soc. Am. **72,** 156–160 (1982).
2. M. Takeda and K. Mutoh, "Fourier transform profilometry for the automatic measurement of 3-D object shapes," Appl. Opt. **22,** 3977–3982 (1983).
3. Y. Morimoto, Y. Seguchi, and T. Higashi, "Application of moiré analysis of strain using Fourier transform," Opt. Eng. **27,** 650–656 (1988).
4. W. W. Macy, Jr., "Two-dimensional fringe-pattern analysis," Appl. Opt. **22,** 3898–3901 (1983).
5. D. J. Bone, H.-A. Bachor, and R. J. Sandeman, "Fringe-pattern analysis using a 2-D Fourier transform," Appl. Opt. **25,** 1653–1660 (1986).
6. C. Roddier and F. Roddier, "Interferogram analysis using Fourier transform techniques," Appl. Opt. **26,** 1668–1673 (1987).
7. E. Ben-Jacob and P. Garik, "The formation of patterns in non-equilibrium growth," Nature (London) **343,** 523–530 (1990).
8. E. Raz, S. G. Lipson, and E. Polturak, "Dendritic growth of ammonium chloride crystals: measurement of the concentration field and a proposed nucleation model for growth," Phys. Rev. A **40,** 1088–1095 (1989).
9. G. T. Herman, *Image Reconstruction from Projections* (Academic, New York, 1980), Chap. 6.